A&A 655, A21 (2021)
https://doi.org/10.1051/0004-6361/202141517

Astronomy & Astrophysics

Three faint-source microlensing planets detected via the resonant-caustic channel

Cheongho Han[1], Andrzej Udalski[2], Doeon Kim[1], Yoon-Hyun Ryu[3], Valerio Bozza[4,5],
Michael D. Albrow[6], Sun-Ju Chung[3,7], Andrew Gould[8,9], Kyu-Ha Hwang[3], Youn Kil Jung[3], Chung-Uk Lee[3],
In-Gu Shin[3], Yossi Shvartzvald[10], Jennifer C. Yee[11], Weicheng Zang[12], Sang-Mok Cha[3,13], Dong-Jin Kim[3],
Hyoun-Woo Kim[3], Seung-Lee Kim[3,7], Dong-Joo Lee[3], Yongseok Lee[3,13], Byeong-Gon Park[3,7], Richard W. Pogge[9]
(The KMTNet Collaboration)
Przemek Mróz[2,14], Michał K. Szymański[2], Jan Skowron[2], Radosław Poleski[2], Igor Soszyński[2], Paweł Pietrukowicz[2],
Szymon Kozłowski[2], Krzysztof Ulaczyk[15], Krzysztof A. Rybicki[2], Patryk Iwanek[2],
Marcin Wrona[2], and Mariusz Gromadzki[2]
(The OGLE Collaboration)

[1] Department of Physics, Chungbuk National University, Cheongju 28644, Republic of Korea
e-mail: cheongho@astroph.chungbuk.ac.kr
[2] Astronomical Observatory, University of Warsaw, Al. Ujazdowskie 4, 00-478 Warszawa, Poland
[3] Korea Astronomy and Space Science Institute, Daejon 34055, Republic of Korea
[4] Dipartimento di Fisica "E. R. Caianiello", Università di Salerno, Via Giovanni Paolo II, 84084 Fisciano (SA), Italy
[5] Istituto Nazionale di Fisica Nucleare, Sezione di Napoli, Via Cintia, 80126 Napoli, Italy
[6] University of Canterbury, Department of Physics and Astronomy, Private Bag 4800, Christchurch 8020, New Zealand
[7] Korea University of Science and Technology, 217 Gajeong-ro, Yuseong-gu, Daejeon 34113, Republic of Korea
[8] Max Planck Institute for Astronomy, Königstuhl 17, 69117 Heidelberg, Germany
[9] Department of Astronomy, The Ohio State University, 140 W. 18th Ave., Columbus, OH 43210, USA
[10] Department of Particle Physics and Astrophysics, Weizmann Institute of Science, Rehovot 76100, Israel
[11] Center for Astrophysics, Harvard & Smithsonian 60 Garden St., Cambridge, MA 02138, USA
[12] Department of Astronomy, Tsinghua University, Beijing 100084, PR China
[13] School of Space Research, Kyung Hee University, Yongin, Kyeonggi 17104, Republic of Korea
[14] Division of Physics, Mathematics, and Astronomy, California Institute of Technology, Pasadena, CA 91125, USA
[15] Department of Physics, University of Warwick, Gibbet Hill Road, Coventry, CV4 7AL, UK

Received 11 June 2021 / Accepted 14 September 2021

ABSTRACT

Aims. We conducted a project of reinvestigating the 2017–2019 microlensing data collected by high-cadence surveys with the aim of finding planets that were missed due to the deviations of planetary signals from the typical form of short-term anomalies.

Methods. The project led us to find three planets, KMT-2017-BLG-2509Lb, OGLE-2017-BLG-1099Lb, and OGLE-2019-BLG-0299Lb. The lensing light curves of the events have a common characteristic: the planetary signals were produced by the crossings of faint source stars over the resonant caustics formed by giant planets located near the Einstein rings of host stars.

Results. For all planetary events, the lensing solutions are uniquely determined without any degeneracy. It is estimated that the host masses are in the range of $0.45 \lesssim M/M_\odot \lesssim 0.59$, which corresponds to early M to late K dwarfs, and thus the host stars are less massive than the Sun. On the other hand, the planets, with masses in the range of $2.1 \lesssim M/M_{\rm J} \lesssim 6.2$, are heavier than the heaviest planet of the Solar System, that is, Jupiter. The planets in all systems lie beyond the snow lines of the hosts, and thus the discovered planetary systems, together with many other microlensing planetary systems, support the idea that massive gas-giant planets are commonplace around low-mass stars. We discuss the role of late-time high-resolution imaging in clarifying resonant-image lenses with very faint sources.

Key words. gravitational lensing: micro – planets and satellites: detection

1. Introduction

During the early phase of planetary microlensing experiments, for example the OGLE (Udalski et al. 1994), MACHO (Alcock et al. 1993), and EROS (Aubourg et al. 1993) surveys, for which the annual detection rate of lensing events was several dozen, individual events could be thoroughly inspected to check the existence of planet-induced anomalies in the light curves of the lensing events. With the advent of high-cadence surveys, that is, MOA (Sumi et al. 2013), OGLE-IV (Udalski et al. 2015), and KMTNet (Kim et al. 2016), the detection rate has soared to more than 3000 per year. With the greatly increased number of events, together with the large quantity of data for each event, planetary signals for some events may escape detection.

Two projects have been carried out since 2020 with the aim of finding missed planets in the survey data collected in and before the 2019 season. One project was conducted to find planet-induced anomalies via an automatized algorithm.

Table 1. Source location, alert date, and baseline magnitude.

Event	(RA, Dec)	(l, b)	Alert date	$I_{\rm base}$
KMT-2017-BLG-2509	(17:42:21.57, −26:19:01.74)	(1°.853, 1°.987)	Postseason	19.96
OGLE-2017-BLG-1099/ KMT-2017-BLG-2336	(17:35:51.42, −29:35:09.10)	(−1°.679, 1°.461)	2017-06-13/ Postseason	20.61
OGLE-2019-BLG-0299/ KMT-2019-BLG-2735	(17:46:43.07,−23:35:03.52)	(4°.702, 2°.570)	2019-03-16/ Postseason	20.04

Hwang et al. (in prep.) applied the automated AnomalyFinder software (Zang et al. 2021) to the 2018–2019 lensing light curves from the ~13 deg^2 of sky covered by the six KMTNet prime fields with cadences ≥2 h^{-1}. From this investigation, they reported six newly detected planets with mass ratios $q < 2 \times 10^{-4}$, OGLE-2019-BLG-1053Lb, KMT-2019-BLG-0253Lb, OGLE-2018-BLG-0506Lb, OGLE-2018-BLG-0516Lb, OGLE-2019-BLG-1492Lb, and OGLE-2018-BLG-0977. The signals of these planets were not only very short but also weak, and thus they had not been noticed from visual inspections. More extensive searches for missing planetary signals via the application of the automated algorithm to all the lensing light curves detected by the KMTNet survey are underway (Jung et al., in prep.).

The other project was conducted by visually inspecting the previous survey data to find unnoticed planetary signals. This project led to the discoveries of ten planets. The first planet was KMT-2018-BLG-0748Lb (Han et al. 2020b), for which the planetary signal had been missed due to the faintness of the source combined with relatively large finite-source effects. This discovery was followed by the detections of: KMT-2016-BLG-2364Lb, KMT-2016-BLG-2397Lb, OGLE-2017-BLG-0604Lb, and OGLE-2017-BLG-1375Lb, for all of which the lensing events involved faint source stars (Han et al. 2021a); KMT-2019-BLG-1339Lb, for which the planetary signal was partially covered (Han et al. 2020a); KMT-2018-BLG-1976Lb, OGLE-2019-BLG-0954Lb, and KMT-2018-BLG-1996Lb, for which the planetary signals were produced through a non-caustic-crossing channel and were thus weak (Han et al. 2021b); and KMT-2018-BLG-1025Lb, for which the planetary signal had been missed due to the low mass ratio of the planet ($q \sim 0.8 \times 10^{-4}$ or 1.6×10^{-4} for two degenerate solutions) together with the non-caustic-crossing nature of its planetary signal (Han et al. 2021c). Visually inspecting missing planets can provide various types of planetary signals that are prone to being missed and thus can help to develop a more complete algorithm for automatized planet detections.

In this paper we report three additional planets with similar planetary signatures and event characteristics found from the (visual) inspection of the 2017–2019 season data collected by the OGLE and KMTNet surveys. The common feature of these planetary events is that the planetary signals were produced by the crossings of faint source stars over the resonant caustics formed by giant planets located near the Einstein rings of the lens systems. Detecting such planetary signals requires a visual inspection of lensing light curves because the durations of the planet-induced anomalies comprise important portions of the event durations, making them difficult to be detected by an automatized system that is optimized to detect very short-term anomalies. An example of such a planetary event is found in the case of OGLE-2016-BLG-0596 (Mróz et al. 2017).

For the presentation of the work, we organize this paper as follows. In Sect. 2 we mention the observations of the lensing events and the acquired data. In Sect. 3 we detail the characteristics of the anomalies in the lensing light curves of the events and describe the detailed analyses conducted to explain the observed anomalies. In Sect. 4 we specify the source types of the events and constrain the angular Einstein radii. In Sect. 5 we determine the physical parameters of the planetary systems using the observables of the events. In Sect. 6 we discuss the role of high-resolution follow-up observations for faint-source planetary events with resonant caustic features in clarifying the nature of the lens system. A summary of the results and conclusion are presented in Sect. 7.

2. Observations and data

The newly reported three planetary lensing events are KMT-2017-BLG-2509, OGLE-2017-BLG-1099/KMT-2017-BLG-2336, and OGLE-2019-BLG-0299/KMT-2019-BLG-2735. The first event was detected solely by the KMTNet survey, and the latter two events were detected by both the OGLE and KMTNet surveys. Hereafter, we designate the events by the identification numbers of the surveys that first found the lensing events. In Table 1 we list the equatorial and galactic coordinates of the source stars, alert dates, and I-band baseline magnitudes, $I_{\rm base}$, of the individual events. The notation "postseason" indicates that the event was detected from the postseason inspection of the data.

After one year of test observations in the 2015 season, the KMTNet group has been carrying out a lensing survey toward the Galactic bulge field since 2016 with the use of three identical 1.6 m telescopes that are distributed on the three continents of the Southern Hemisphere, at the Siding Spring Observatory in Australia, the Cerro Tololo Interamerican Observatory in Chile, and the South African Astronomical Observatory in South Africa. We designate the individual telescopes as KMTA, KMTC, and KMTS, respectively. The camera mounted on each telescope has a 4 deg^2 field of view. The OGLE team has been conducting a lensing survey since its commencement of the first phase experiment in 1992 (Udalski et al. 1994), and now the survey is in the fourth phase (OGLE-IV); it now uses an upgraded camera that yields a 1.4 deg^2 field of view (Udalski et al. 2015). The OGLE telescope with an aperture of 1.3 m is located at the Las Campanas Observatory in Chile. For both surveys, images of the events were obtained mainly in the I band, and a fraction of V-band images were acquired for the source color measurements. In Table 2 we list the data sets used in the analysis, the fields of the individual surveys, and the cadence of observations. We note that the KMTNet cadences of the events, ranging from 1.0–2.5 h, are substantially lower than the cadence of the prime fields, 15 min, and this partially contributed to the difficulty in identifying the planetary nature of the events.

The data used in the analyses were reduced using the photometry pipelines of the individual survey groups. These

Table 2. Data sets, fields, and observational cadences.

Event	Data sets	Field	Cadence
KMT-2017-BLG-2509	KMTA, KMTC, KMTS	KMT18	1 h
OGLE-2017-BLG-1099	OGLE,	BLG654.2	1/3–1 day
	KMTA, KMTC, KMTS	KMT14	1 h
OGLE-2019-BLG-0299	OGLE,	BLG632.10	1/3–1 day
	KMTA, KMTC, KMTS	KMT20	2.5 h

Table 3. Error adjustment factors.

Event	Data set	k	$\sigma_{\rm min}$ (mag)	$N_{\rm data}$
KMT-2017-BLG-2509	KMTA	1.054	0.020	200
	KMTC	1.330	0.020	489
	KMTS	1.192	0.020	430
OGLE-2017-BLG-1099	OGLE	1.179	0.010	366
	KMTA	1.149	0.020	139
	KMTC	1.054	0.010	183
	KMTS	1.025	0.030	225
OGLE-2019-BLG-0299	OGLE	1.265	0.010	249
	KMTA	1.195	0.040	53
	KMTC	1.545	0.020	395
	KMTS	1.179	0.020	354

pipelines, developed by Albrow et al. (2009) for KMTNet and by Woźniak (2000) for OGLE, utilize the difference imaging technique (Tomaney & Crotts 1996; Alard & Lupton 1998), which is optimized for the photometry of stars in very dense star fields. A subset of the KMTC data was additionally processed using the pyDIA photometry code (Albrow 2017) to construct color-magnitude diagrams (CMDs) of stars around the source stars and to specify the source types (see Sect. 4 for details). For the data used in the analyses, we readjusted the error bars of the photometric data by $\sigma = k(\sigma_{\rm min}^2 + \sigma_0^2)^{1/2}$ following the prescription outlined in Yee et al. (2012). Here, σ_0 denotes the error bar from the pipelines, $\sigma_{\rm min}$ is a factor used to make the scatter of data consistent with error bars, and k is a scaling factor used to make the χ^2 per degree of freedom for each data set equal to unity. In Table 3 we list the error-bar readjustment factors and the number of data, $N_{\rm data}$, of the individual data sets.

3. Analysis

In this section we present the detailed analyses of the individual lensing events. The light curves of all events exhibit anomaly features that include caustic crossings, and thus we model the light curves under a binary-lens and single-source (2L1S) interpretation.

The modeling was done by searching for the set of the lensing parameters that best explains the observed data. The first three of these parameters describe the source–lens approach, including $(t_0, u_0, t_{\rm E})$, which represent the time of the closest source approach to a reference position of the lens, the separation (normalized to the angular Einstein radius, $\theta_{\rm E}$) between the source and the lens reference position at t_0, and the event timescale, respectively. For the reference position of the lens, we used the center of mass for a binary lens with a separation less than $\theta_{\rm E}$ (close binary), and we used the effective position, defined by Di Stefano & Mao (1996) and An & Han (2002), for the lens with a separation greater than $\theta_{\rm E}$ (wide binary). The next three parameters (s, q, α) describe the lens binarity, and they denote the projected separation (normalized to $\theta_{\rm E}$) and mass ratio between the lens components, M_1 and M_2, and the angle between the source motion and the binary axis (source trajectory angle), respectively. The last parameter is ρ, which is defined as the ratio of the angular source radius, θ_*, to $\theta_{\rm E}$, that is, $\rho = \theta_*/\theta_{\rm E}$ (normalized source radius), and it is included to account for finite-source effects that affect the caustic-crossing parts of lensing light curves. We incorporated limb-darkening effects in the finite magnification computations by modeling the surface brightness variation of the source as $S \propto 1 - \Gamma(1-3\cos\phi/2)$, where Γ is the limb-darkening coefficient and ϕ represents the angle between two lines extending from the source center: one to the observer and the other to the source surface. As will be discussed in Sect. 4, the source stars of all events are of similar spectral types, early K-type main-sequence stars, and thus we adopted an I-band limb-darkening coefficient of $\Gamma_I = 0.5$ from Claret (2000), assuming that the effective temperature, surface gravity, and turbulence velocity are $T_{\rm eff} = 5000$ K, $\log(g/g_\odot) = 0.05$, and $v_{\rm turb} = 2$ km s^{-1}, respectively.

For a fraction of events with long timescales comprising an important portion of a year, lensing light curves may deviate from the form expected from a rectilinear lens-source motion. One cause for this deviation is the motion of an observer induced by the orbital motion of Earth (microlens-parallax effect; Gould 1992), and the other is the orbital motion of the binary lens (lens-orbital effects; Dominik 1998). It is expected that the signature of the microlens parallax, $\pi_{\rm E}$, will be small for OGLE-2017-BLG-1099 and OGLE-2019-BLG-0299 due to their short timescales, which are ~19 days and ~30 days, respectively, but the signature might not be small for KMT-2017-BLG-2509 due to its relatively long timescale of ~67 days. We checked these higher-order effects and found that it is difficult to detect the higher-order signatures for any of the events, mainly because the photometric quality is not high enough to detect the subtle deviations induced by these higher-order effects. A microlens parallax can provide an important constraint on the physical lens parameters. As will be discussed in Sect. 5, the uncertainties of the physical lens parameters are large for all events due to the absence of the $\pi_{\rm E}$ constraint.

The 2L1S modeling was carried out in two steps. In the first step, the binary lensing parameters s and q were searched for using a grid approach with different starting values of α evenly distributed in the $0 - 2\pi$ range with 21 grids, while the five non-grid lensing parameters, that is, $(t_0, u_0, t_{\rm E}, \alpha, \rho)$, were found using a downhill approach based on the Markov chain Monte Carlo (MCMC) algorithm. The ranges of the grid parameters

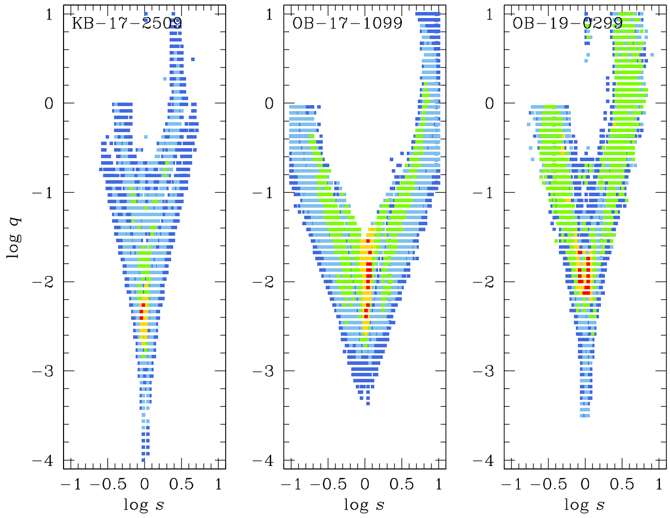

Fig. 1. $\Delta\chi^2$ maps on the $\log s$–$\log q$ parameter plane obtained from the first-round modeling of the individual events. Color coding is set to represent points with $\Delta\chi^2 \leq n(1^2)$ (red), $\Delta\chi^2 \leq n(2^2)$ (yellow), $\Delta\chi^2 \leq n(3^2)$ (green), $\Delta\chi^2 \leq n(4^2)$ (cyan), and $\Delta\chi^2 \leq n(5^2)$ (blue), where $n = 5$, 3, and 9 for KMT-2017-BLG-2509, OGLE-2017-BLG-1099, and OGLE-2019-BLG-0299, respectively.

are $-1.0 \leq \log s < 1.0$ and $-4.0 \leq \log q < 1.0$, and they were divided into 70 grids. We then identified local solutions that appear in the $\Delta\chi^2$ map on the s–q parameter plane. In the second step, we refined the individual local solutions found in the first step by letting all parameters vary. Then, the global solution was found by comparing χ^2 values of the local solutions if there were more than one. Figure 1 shows the $\Delta\chi^2$ maps on the $\log s$–$\log q$ parameter plane obtained from the first-step modeling of the individual events. It shows that there exists a single local solution for all events.

3.1. KMT-2017-BLG-2509

Figure 2 shows the lensing light curve of KMT-2017-BLG-2509. It is characterized by two distinctive caustic features that appear at $t_1 \sim 7858$ and $t_2 \sim 7870$ in HJD′ ≡ HJD − 2 450 000. For the first caustic feature, both the rising side (covered by four KMTA data points) and the falling side (covered by a single KMTC point) were captured, while only the rising side was covered (by five KMTC points) for the second feature (see the zoomed-in view of the anomaly region shown in Fig. 3). The region between the two caustic features exhibits negative deviations from a single-lens single-source (1L1S) light curve. Regarding the light curve, it should be noted that the error bars of the data are substantial due to the faintness of the source and that the anomaly region occupies a large portion of the magnified region of the light curve. This made it difficult for the anomalies to be readily noticed as a planetary (rather than a stellar-binary) signal[1].

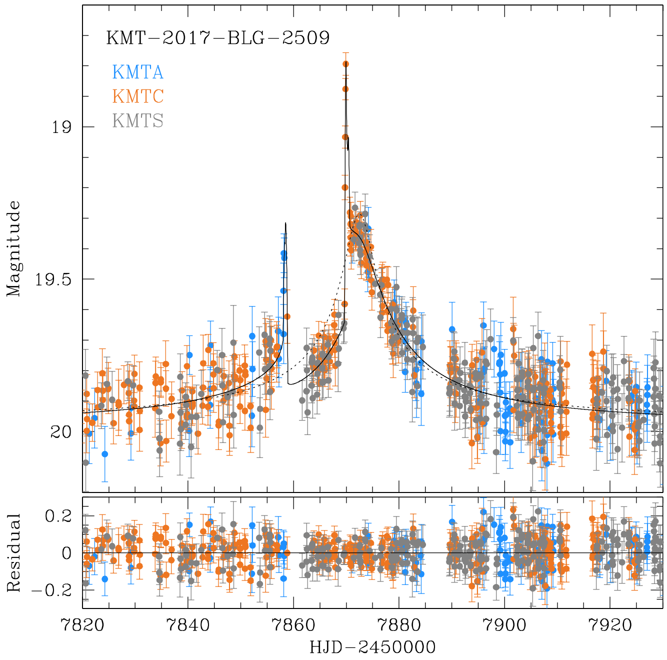

Fig. 2. Light curve of KMT-2017-BLG-2509. The dotted and solid curves plotted over the data points represent the 1L1S and 2L1S models, respectively. The residual of the 2L1S model is shown in the *lower panel*. The colors of the telescopes in the legend are set to match those of the data points.

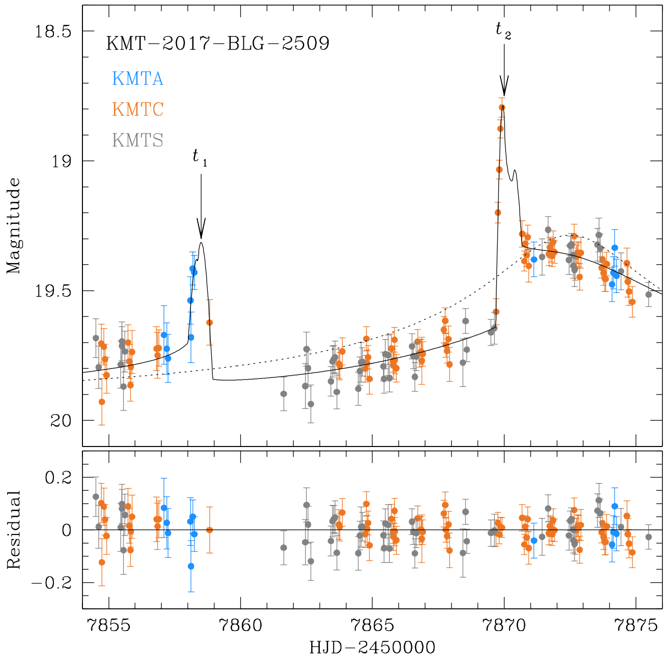

Fig. 3. Zoomed-in view of the major anomaly region of KMT-2017-BLG-2509. Notations are the same as those in Fig. 2.

The 2L1S modeling yields binary parameters of $(s, q) \sim (0.93, 4.4 \times 10^{-3})$, indicating that the companion to the primary lens is a planetary-mass object lying near the Einstein ring of the primary. We find a unique solution without any degeneracy. For a lensing event produced by a binary lens with a small mass ratio, there often exists a pair of close

---

[1] The caustic morphology and mass ratio of KMT-2017-BLG-2509 are similar to those of MOA-2009-BLG-387 (Batista et al. 2011). When there were relatively few microlensing events being discovered, MOA-2009-BLG-387 was easily identified as a planet, while the planetary nature of KMT-2017-BLG-2509 had not been noticed until this paper. This indicates that a more rigorous review of anomalies in the previous microlensing data is important for the accurate estimation of microlensing planet statistics.

Table 4. Lensing parameters.

Parameter	KMT-2017-BLG-2509	OGLE-2017-BLG-1099	OGLE-2019-BLG-0299
t_0 (HJD′)	7872.205 ± 0.158	7917.336 ± 0.004	8560.239 ± 0.025
u_0	0.066 ± 0.007	0.004 ± 0.001	0.056 ± 0.002
t_E (days)	67.39 ± 5.37	18.87 ± 1.57	29.82 ± 1.05
s	0.925 ± 0.007	1.137 ± 0.014	0.990 ± 0.002
q (10^{-3})	4.366 ± 0.534	6.420 ± 0.779	10.037 ± 0.637
α (rad)	2.531 ± 0.027	0.065 ± 0.014	1.277 ± 0.0186
ρ (10^{-3})	1.927 ± 0.301	1.539 ± 0.166	<3.5
f_s	0.008 ± 0.001	0.012 ± 0.001	0.065 ± 0.002
f_b	0.155 ± 0.001	0.137 ± 0.001	0.018 ± 0.002

Notes. HJD′ ≡ HJD − 2 450 000.

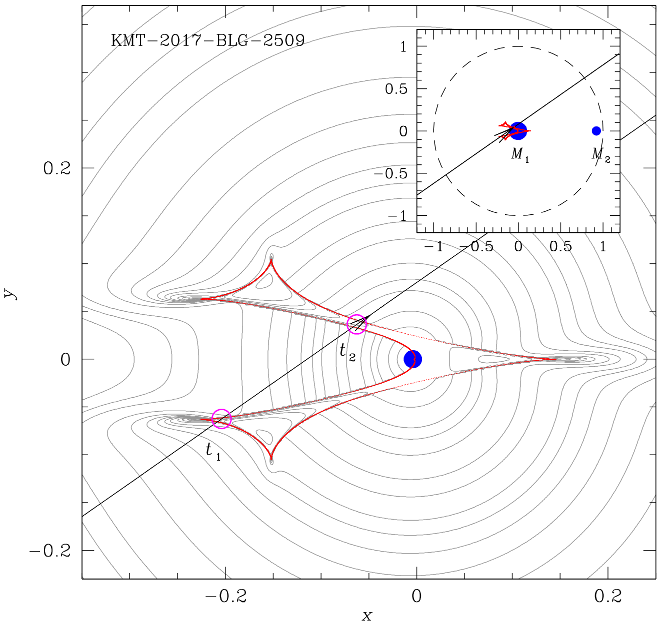

Fig. 4. Lens system configuration of KMT-2017-BLG-2509. The inset shows the whole view of the lens system, and the main panel shows the enlarged view around the caustic. The red closed figure is the caustic, the line with an arrow represents the source motion, the two filled blue dots indicate the positions of the lens components, and the dashed circle is the Einstein ring. The gray curves around the caustic represent equi-magnification contours. The empty magenta dots on the source trajectory represent the source positions at t_1 and t_2, marked in Fig. 2. The size of the dot is not scaled to the source size.

($s < 1.0$) and wide ($s > 1.0$) solutions arising from the similarity between the central caustics induced by the companions with s and s^{-1}: the close–wide degeneracy (Griest & Safizadeh 1998; Dominik 1999). It is found that KMT-2017-BLG-2509 is not subject to this degeneracy because the light-curve morphology (two pairs of caustic crossings that flank a de-magnified region) is strictly characteristic of an $s < 1$ geometry (see Fig. 4). The normalized source radius, $\rho \sim 1.9 \times 10^{-3}$, is measured by analyzing the caustic-crossing parts of the light curve.

The model curve of the 2L1S solution is drawn over the data points in Figs. 2 and 3. In Table 4 we list the full lensing parameters of the model together with the flux parameters of the source, f_s, and blend, f_b, in which the flux is approximately scaled to that of $I = 18$, that is, $f = 10^{-0.4(I-18)}$. Figure 4 shows the configuration of the lens system corresponding to the solution. The planet is located close to the Einstein ring, and this results in a single, six-sided resonant caustic. The caustic appears as the merging of the single central caustic and the two sets of planetary caustics. The source crossed the tip of the lower planetary caustic at t_1 and then crossed the slim bridge connecting the upper planetary caustic and the central caustic at t_2. The negative deviation region between t_1 and t_2 occurred when the source passed through the negative deviation region formed between the two planetary caustics.

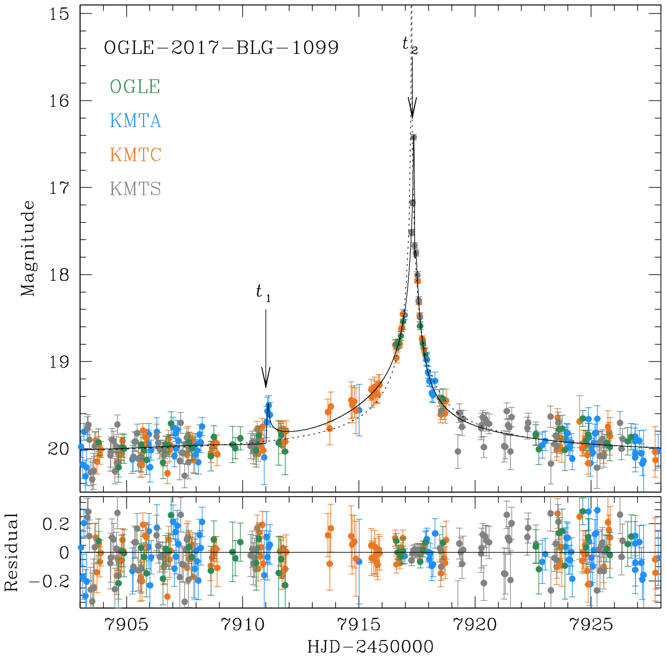

Fig. 5. Light curve of OGLE-2017-BLG-1099. Notations are the same as those in Fig. 2.

3.2. OGLE-2017-BLG-1099

The lensing light curve of OGLE-2017-BLG-1099 is shown in Fig. 5. The online data of the event posted on the alert web pages of the individual survey groups[2] did not show an obvious anomaly feature in the light curve. Nevertheless, the event was

---

[2] `http://ogle.astrouw.edu.pl/ogle4/ews/ews.html` for the OGLE survey and `https://kmtnet.kasi.re.kr/~ulens/` for the KMTNet survey.

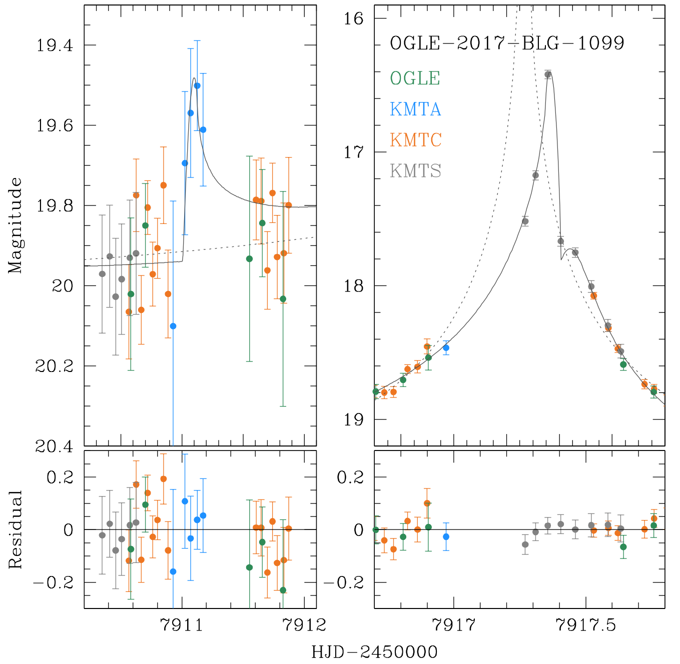

Fig. 6. Zoomed-in view of the major anomaly region of OGLE-2017-BLG-1099.

selected for a detailed analysis because it reached a very high magnification, $A_{\rm max} \sim 140$, during which the chance of detecting a planet-induced anomaly was high (Griest & Safizadeh 1998). The optimal light curve obtained by re-reducing the data revealed that the light curve was anomalous. The anomaly is characterized first by the asymmetry of the light curve and second by the caustic-involved feature at $t_2 \sim 7917.4$. The zoomed-in view of the region around t_2 presented in the right panel of Fig. 6 shows that the five KMTS data points exhibit the characteristic pattern of magnification variation that occurs when a source exits a caustic (see Fig. 1 of Gould & Andronov 1999).

The 2L1S modeling yields a unique solution with the binary parameters of $(s, q) \sim (1.1, 6.4 \times 10^{-3})$, indicating that the companion is a planetary-mass object with a separation similar to $\theta_{\rm E}$. We note that the analysis of the event was done in the 2017 season and that its planetary nature was realized by one of the coauthors (Y.-H. Ryu), but the result was not shared with the other coauthors. As a result, the analysis presented in this work was carried out independently, reaching a result that is consistent with the previous one. The full lensing parameters are listed in Table 4, and the model curve is presented in Figs. 5 and 6. Due to the proximity of the binary separation to unity, the binary lens pair forms a single resonant caustic. According to the model, the source entered the caustic at $t_1 \sim 7911$ and exited the caustic at t_2. Due to the weakness of the caustic combined with the low photometric precision, it was difficult to notice the anomaly feature that occurred at around the caustic entrance in the preliminary modeling using the online data, but the re-reduced data showed that the caustic was covered by four KMTA data points, although the uncertainties of the data points around the caustic were still large (see the zoomed-in view around t_1 shown in the left panel of Fig. 6). The coverage of both the caustic entrance and exit yields a normalized source radius of $\rho \sim 1.5 \times 10^{-3}$.

Figure 7 shows the configuration of the lens system. As in the case of KMT-2017-BLG-2509, the caustic appears as the merging of the planetary and central caustics. The source moved approximately in parallel with the binary axis ($\alpha \sim 3.7°$). It entered the caustic by passing the lower right side of the planetary caustic, generating a weak caustic spike at t_1. Then, the source exited the caustic by passing the left side of the central caustic and then passed the region close to the back-end cusp of the central caustic, and this produced the caustic feature at t_2 (see the zoomed-in view of the central region presented in the left inset).

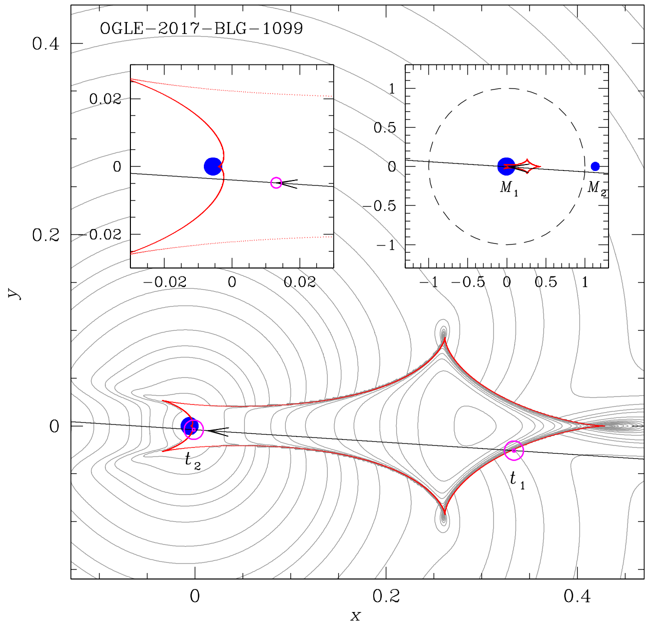

Fig. 7. Lens system configuration of OGLE-2017-BLG-1099. Notations are the same as those in Fig. 4, except that an additional inset (*left*) is presented to show a zoomed-in view of the central region. The source positions corresponding to t_1 and t_2 designated in Fig. 5 are marked by the empty magenta dots. The size of the dot in the main panel is arbitrary, but the dot in the left inset is scaled to the source size.

3.3. OGLE-2019-BLG-0299

Figure 8 shows the light curve of OGLE-2019-BLG-0299. The anomalous nature of the light curve was known when the event was proceeding, and planetary-lensing models found with the use of the OGLE data were circulated to the microlensing community by C. Han and V. Bozza before the end of the event. The analysis in this work was done with the addition of the KMTNet data obtained from the optimized photometry of the event. The enlarged view of the light curve around the anomaly region is shown in Fig. 9. The anomaly exhibits a very complex pattern that is characterized by six peaks or bumps, at $t_1 \sim 8556.2$, $t_2 \sim 8556.7$, $t_3 \sim 8559.4$, $t_4 \sim 8560.5$, $t_5 \sim 8562.5$, and $t_6 \sim 8563.5$.

A 2L1S modeling yields a unique solution with the binary parameters of $(s, q) \sim (0.99, 10.0 \times 10^{-3})$. The binary separation is very close to unity, as in the cases of the two previous events. The mass ratio is about ten times the Jupiter/Sun ratio of the Solar System, but the mass of the companion is still in the planet-mass regime, considering that the measured event timescale, $t_{\rm E} \sim 30$ days, is not much longer than those of typical lensing events produced by low-mass stars. The full lensing parameters are presented in Table 4. Although all the major anomaly features were delineated, none of the caustics was resolved densely

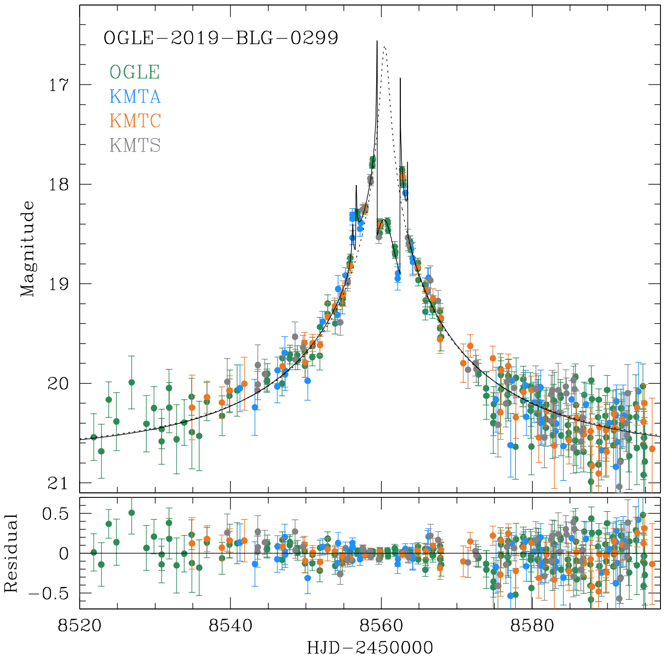

Fig. 8. Lensing light curve of OGLE-2019-BLG-0299. Notations are the same as those in Fig. 2.

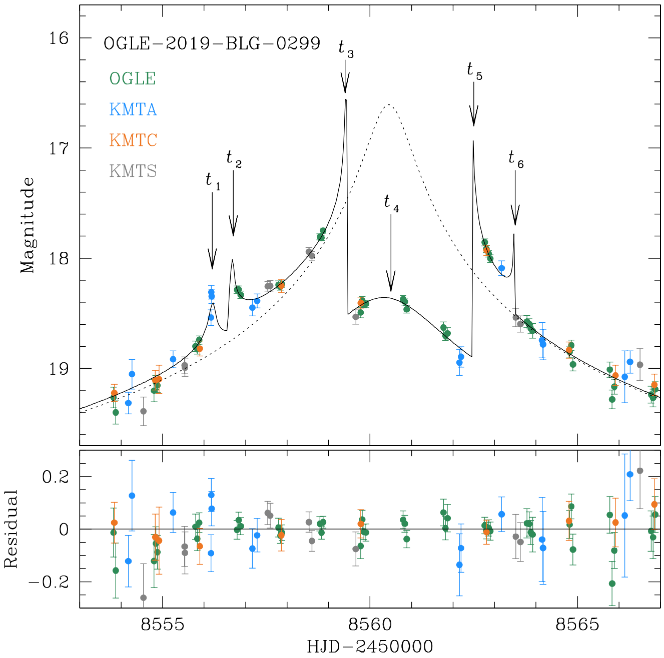

Fig. 9. Enlarged view around the anomaly region of the OGLE-2019-BLG-0299 light curve. The positions marked by arrows and labeled as t_1, t_2, t_3, t_4, t_5, and t_6 represent the epochs of major anomaly features.

enough for the secure measurement of ρ, and only the upper limit, $\rho_{\rm max} \sim 3.5 \times 10^{-3}$, is constrained.

Figure 10 shows the lens system configuration of OGLE-2019-BLG-0299. According to the model, the source crossed the binary axis with a source trajectory angle of $\alpha \sim 73^\circ$ and passed through the six-fold resonant caustic four times, at t_2, t_3, t_5, and t_6, where (t_2, t_3) and (t_5, t_6) are the two time pairs of caustic entrance and exit. These caustic crossings produced the spikes at the corresponding times, and the regions of the light curve between the individual caustic-crossing pairs exhibited characteristic U-shape trough patterns. The bump at t_1 was produced by the source approach close to the lower cusp of the caustic before the first caustic crossing at t_2. The other bump, at t_4, was produced when the source passed through the outer-caustic region near the left-side on-axis cusp of the caustic. The source positions corresponding to the six epochs of the anomaly are marked by empty magenta dots (not to scale) on the source trajectory.

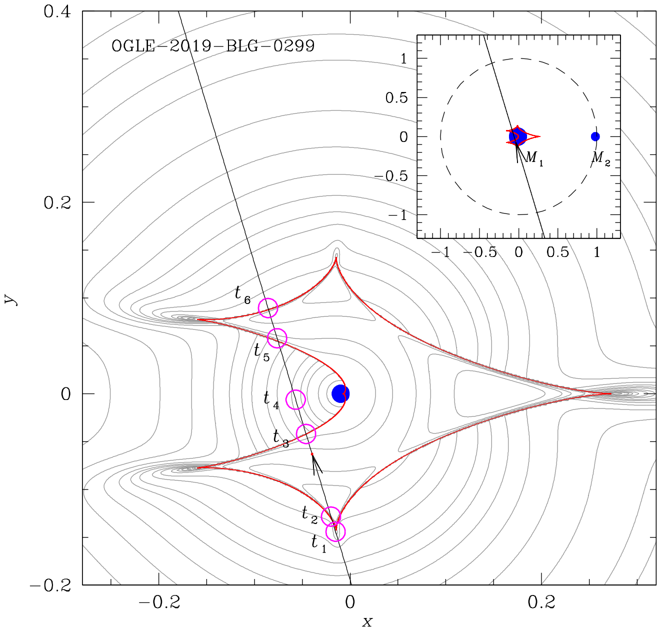

Fig. 10. Lens system configuration of OGLE-2019-BLG-0299. The empty magenta points represent the source positions corresponding to the six epochs of t_1, t_2, t_3, t_4, t_5, and t_6 that are marked by arrows in Fig. 9. The size of the dots is not scaled.

4. Source stars and Einstein radii

In this section we estimate the angular Einstein radii of the events. The Einstein radius was determined by $\theta_{\rm E} = \theta_*/\rho$. The ρ value was measured or constrained from the analysis of the caustic-crossing parts, which are affected by finite-source effects. With the measured ρ, it was then required to estimate the angular source radius, θ_*. The value of θ_* was deduced from the color and magnitude of the source.

In general, the source color is estimated by measuring the source magnitudes in two passbands, the I and V bands in our case, which in turn is done by regressing the data of the individual passbands with the variation of the lensing magnification. The I-band magnitudes were securely measured by this method for all events. However, measuring the V-band magnitudes is difficult with this method due to the large uncertainties of the data, making it difficult to securely estimate the source colors. We, therefore, estimated the source color using the Bennett et al. (2008) method, which utilizes the CMD constructed from the *Hubble* Space Telescope (HST) observations (Holtzman et al. 1998). In the first step of this method, the HST CMD is aligned with the CMD obtained from ground-based observations using the well-defined centroid of the red giant clump (RGC). In the second step, the source position in the CMD is interpolated from the branch of main-sequence or giant stars on the HST CMD

Table 5. Source color, magnitude, radius, Einstein radius, and proper motion.

Quantity	KMT-2017-BLG-2509	OGLE-2017-BLG-1099	OGLE-2019-BLG-0299
$(V-I, I)$	$(3.482 \pm 0.186, 23.013 \pm 0.077)$	$(3.751 \pm 0.172, 22.795 \pm 0.069)$	$(2.488 \pm 0.126, 20.986 \pm 0.039)$
$(V-I, I)_{\rm RGC}$	$(3.401, 17.277)$	$(3.785, 17.327)$	$(2.653, 15.974)$
$(V-I, I)_{\rm RGC,0}$	$(1.060, 14.441)$	$(1.060, 14.445)$	$(1.060, 14.439)$
$(V-I, I)_0$	$(1.141 \pm 0.186, 20.177 \pm 0.077)$	$(1.026 \pm 0.172, 19.912 \pm 0.069)$	$(0.894 \pm 0.126, 19.451 \pm 0.039)$
θ_* (µas)	0.47 ± 0.09	0.47 ± 0.09	0.50 ± 0.07
$\theta_{\rm E}$ (mas)	0.243 ± 0.110	0.304 ± 0.125	>0.14
μ (mas yr^{-1})	1.32 ± 0.60	5.89 ± 2.47	>1.74

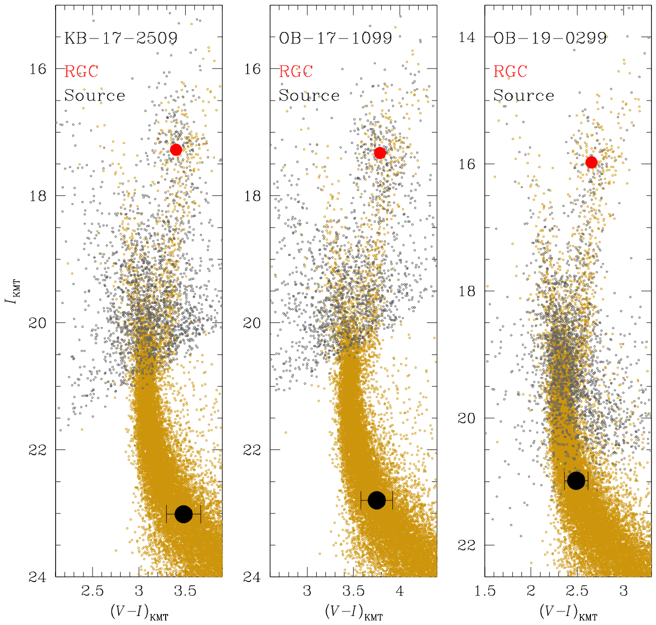

Fig. 11. Source positions (filled black dot with error bars) in the instrumental CMD with respect to the centroids of the RGC (filled red dots) for the individual lensing events. In each panel, the ground-based and HST CMDs are marked by gray and brown dots, respectively.

using the well-measured I-band magnitude difference between the RGC centroid and the source. In the final step, the source color and its uncertainty are estimated as the mean and standard deviation of stars located on the branch.

Figure 11 shows the source locations (black filled dots with error bars) with respect to the RGC centroids (red filled dot) in the combined CMD. In Table 5 we list the positions of the source, $(V-I, I)$, and the RGC centroid, $(V-I, I)_{\rm RGC}$, measured on the instrumental CMD. The reddening and extinction corrected (de-reddened) color and magnitude of the source, $(V-I, I)_0$, were then determined using the offsets from the RGC centroid, $\Delta(V-I, I)$, together with the known de-reddened values of RGC, $(V-I, I)_{\rm RGC,0}$ (Bensby et al. 2013; Nataf et al. 2013), by the relation

$$(V-I, I)_0 = (V-I, I)_{\rm RGC,0} + \Delta(V-I, I). \tag{1}$$

The values of $(V-I, I)_0$, $\Delta(V-I, I)$, $(V-I, I)_{\rm RGC,0}$ for the individual events are listed in Table 5. We note that the de-reddened I-band magnitudes of the RGC centroids, that is, $I_{\rm RGC,0}$, vary depending on the event because we consider the varying distance depending on the source location using Table 1 of Nataf et al. (2013). The measured colors and magnitudes, which are in the ranges of $0.9 \lesssim (V-I)_0 \lesssim 1.1$ and $19.5 \lesssim I_0 \lesssim 20.2$, respectively, indicate that the source stars of the events are of similar spectral types, early K-type main-sequence stars.

The measured $(V-I)$ color was then converted into $(V-K)$ color using the color-color relation of Bessell & Brett (1988), and then the source radius was deduced from the $(V-K)$–θ_* relation of Kervella et al. (2004). With the measured source radius, the Einstein radius and the relative lens-source proper motion were then estimated using the relations $\theta_{\rm E} = \theta_*/\rho$ and $\mu = \theta_{\rm E}/t_{\rm E}$, respectively. We list the estimated values of θ_*, $\theta_{\rm E}$, and μ in Table 5. We note that the lower limits $\theta_{\rm E}$ and μ are presented for OGLE-2019-BLG-0299 because only the upper limit of ρ is constrained for the event.

5. Physical lens parameters

We estimated the physical lens parameters of the lens mass, M, and distance, $D_{\rm L}$, by conducting a Bayesian analysis. The lensing observables that can be used to constrain M and $D_{\rm L}$ include $t_{\rm E}$, $\theta_{\rm E}$, and $\pi_{\rm E}$, where the first two observables are related to M and $D_{\rm L}$ by

$$t_{\rm E} = \frac{\theta_{\rm E}}{\mu};\quad \theta_{\rm E} = (\kappa M \pi_{\rm rel})^{1/2};\quad \pi_{\rm rel} = {\rm AU}\left(\frac{1}{D_{\rm L}} - \frac{1}{D_{\rm S}}\right), \tag{2}$$

and the additional measurement of $\pi_{\rm E}$ would allow one to uniquely determine the lens parameters by

$$M = \frac{\theta_{\rm E}}{\kappa \pi_{\rm E}};\qquad D_{\rm L} = \frac{\rm AU}{\pi_{\rm E}\theta_{\rm E} + \pi_{\rm S}}. \tag{3}$$

Here, $\kappa = 4G/(c^2{\rm AU})$, $\pi_{\rm S} = {\rm AU}/D_{\rm S}$, and $D_{\rm S}$ denotes the distance to the source (Gould 2000). The available observables vary depending on the events: $t_{\rm E}$ and $\theta_{\rm E}$ for KMT-2017-BLG-2509 and OGLE-2017-BLG-1099, and $t_{\rm E}$ and the lower limit of $\theta_{\rm E}$ for OGLE-2019-BLG-0299. The value of $\pi_{\rm E}$ is not measured for any of the events.

In the first step of the Bayesian analysis, we produced artificial lensing events by conducting a Monte Carlo simulation. In the simulation, we used a prior Galactic model, which describes the physical and dynamical distributions and the mass function of Galactic objects. We adopted the Jung et al. (2021) Galactic model, in which the physical distribution of disk and bulge objects are described by the Robin et al. (2003) and Han & Gould (2003) models, respectively, the dynamical distributions of the disk and bulge objects are depicted by the Jung et al. (2021) and Han & Gould (1995) models, respectively, and the Jung et al. (2018) mass function model is commonly used for both populations. In the second step, we chose events with $t_{\rm E}$ and $\theta_{\rm E}$ values consistent with the measured observables and constructed the posterior distributions of M and $D_{\rm L}$ for these events.

Table 6. Physical lens parameters.

Parameter	KMT-2017-BLG-2509	OGLE-2017-BLG-1099	OGLE-2019-BLG-0299
1 $M_{\rm planet}$ ($M_{\rm J}$)	$2.09^{+1.68}_{-1.26}$	$3.02^{+2.43}_{-1.81}$	$6.22^{+3.80}_{-3.67}$
$M_{\rm host}$ ($M_\odot$)	$0.46^{+0.37}_{-0.27}$	$0.45^{+0.36}_{-0.27}$	$0.59^{+0.36}_{-0.35}$
$D_{\rm L}$ (kpc)	$7.04^{+0.89}_{-1.27}$	$7.25^{+1.06}_{-1.40}$	$5.83^{+1.21}_{-1.85}$
$a_\perp$ (AU)	$2.14^{+0.27}_{-0.39}$	$2.73^{+0.40}_{-0.53}$	$2.80^{+0.58}_{-0.89}$

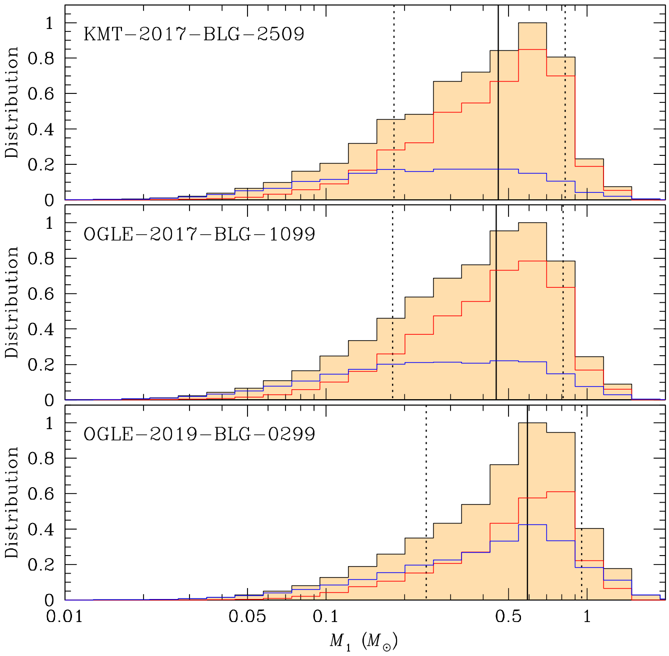

Fig. 12. Bayesian posteriors of the primary lens mass, M_1, for KMT-2017-BLG-2509 (*top panel*), OGLE-2017-BLG-1099 (*middle panel*), and OGLE-2019-BLG-0299 (*bottom panel*). In each panel, the blue and red curves represent the contributions by the disk and bulge lens populations, respectively, and the black curve represents the sum of the two lens populations. The solid vertical line represents the median, and the two dotted lines indicate the 1σ range of the distribution.

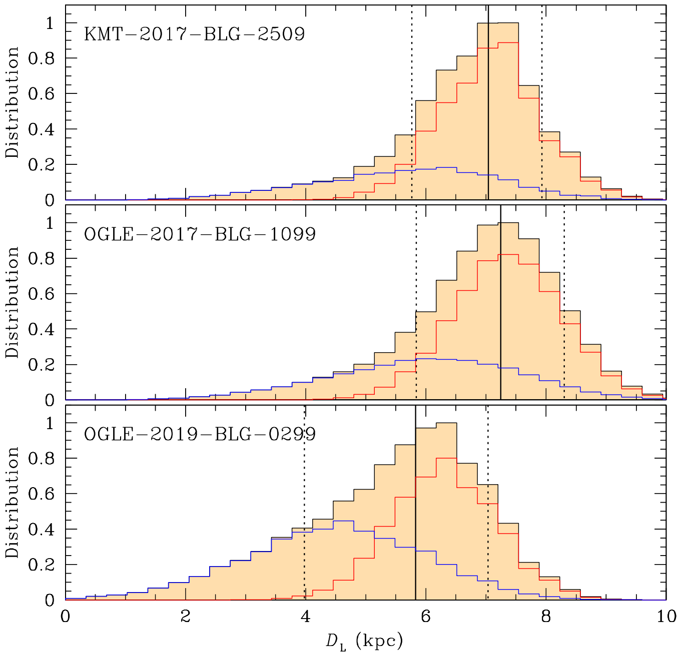

Fig. 13. Bayesian posteriors of the lens distance, $D_{\rm L}$. Notations are the same as those in Fig. 12.

Then, the representative values of the lens parameters were determined as the median values of the posterior distributions, and the lower and upper limits were determined as 16 and 84% of the distributions, respectively.

In Figs. 12 and 13 we present the Bayesian posterior distributions of M_1 and $D_{\rm L}$, respectively. In Table 6 we list the estimated masses of the host ($M_{\rm host} \equiv M_1$) and planet ($M_{\rm planet} \equiv M_2$), the distance, and the projected planet-host separation ($a_\perp$). The projected separation was calculated by $a_\perp = sD_{\rm L}\theta_{\rm E}$. It is estimated that the host masses are in the range of $0.45 \lesssim M_{\rm host}/M_\odot \lesssim 0.59$, which corresponds to early M to late K dwarfs, and thus the host stars are less massive than the Sun. On the other hand, the planet masses, which are in the range of $2.1 \lesssim M_{\rm planet}/M_{\rm J} \lesssim 6.2$, are heavier than the mass of the heaviest planet of the Solar System, that is, Jupiter. Considering that the snow line distance is $a_{\rm sl} \sim 2.7(M/M_\odot)$ AU and that $a_\perp$ is the separation in projection, the planets in all systems lie beyond the snow lines of the hosts. Therefore, the discovered planetary systems, together with many other microlensing planetary systems, support the idea that massive gas-giant planets are commonplace around low-mass stars (see the distribution of exoplanets with respect to $a_\perp/a_{\rm sl}$ presented in Fig. 6 of Gaudi 2012). The disk and bulge contributions are, respectively, 28 and 72% for KMT-2017-BLG-2509, 33 and 67% for OGLE-2017-BLG-1099, and 48 and 52% for OGLE-2019-BLG-0299. The relatively low disk contribution for KMT-2017-BLG-2509 arises due to the constraint of the low relative lens-source proper motion, $\mu \sim 1.3$ mas yr^{-1}, because low proper motion is difficult to produce for disk lenses.

6. High-resolution follow-up observation

In the general case of a lensing event, high-resolution observations using space-borne telescopes or ground-based adaptive optics instruments allow one to measure the lens flux and the lens-source separation. The lens flux allows one to estimate the lens mass, M, and the lens-source separation allows one to estimate the relative lens-source proper motion, μ, which in turn constrains the Einstein radius by $\theta_{\rm E} = \mu t_{\rm E}$.

For faint-source planetary lensing events with resonant caustic features, high-resolution follow-up observations are especially important for clarifying the planetary lens systems. The size of a resonant planetary caustic scales to the planet/host mass ratio as $\Delta\zeta_{\rm c} \propto q^{1/3}\theta_{\rm E}$, and thus the duration of the planetary anomaly is related to the event timescale by $\Delta t = \Delta\zeta_{\rm c}/\mu \propto q^{1/3}t_{\rm E}$.

For a given anomaly duration, then, the event timescale and the mass ratio are related by $q \propto t_{\rm E}^{-3}$. For faint-source events, the very faint sources can make it difficult to precisely determine $t_{\rm E}$, and this leads to a large uncertainty of q because $\Delta q \propto 3\Delta t_{\rm E}$. Late-time observations in two passbands can yield the source flux and color and, thus, the I-band source-flux estimate. The well-estimated source flux can further constrain $t_{\rm E}$, and this leads to a tight constraint on the planet mass ratio. High-resolution image data could have resulted in best constraints if they had been acquired at the time of the event to provide a comparison. Unfortunately, no such images were taken because the planetary nature of the events was not known at the times of the event discoveries. However, post-event imaging can still help to constrain the physical parameters of the lens systems.

7. Summary and conclusion

We have reported three microlensing planets, KMT-2017-BLG-2509Lb, OGLE-2017-BLG-1099Lb, and OGLE-2019-BLG-0299Lb, that were found from the reinvestigation of the microlensing data collected by the KMTNet and OGLE surveys during the 2017–2019 seasons. For all of these lensing events, the planetary signals deviated from the typical form of short-term anomalies because they were produced by the crossings of the source stars over the resonant caustics formed by the giant planets located around the Einstein rings of host stars. The faintness of the source stars and the relatively low observational cadences also contributed to the difficulty in finding the planetary signals. Due to the resonant nature of the caustics, the lensing solutions were uniquely determined without any degeneracy. The estimated masses of the planet hosts are in the range of $0.45 \lesssim M/M_\odot \lesssim 0.59$, which corresponds to early M to late K dwarfs, and thus the host stars are less massive than the Sun. On the other hand, the planets, with masses in the range of $2.1 \lesssim M_{\rm planet}/M_{\rm J} \lesssim 6.2$, are heavier than Jupiter. The planets in all systems lie beyond the snow lines of the hosts, and thus the discovered planetary systems support the conclusion that massive gas-giant planets are commonplace around low-mass stars.

Acknowledgements. Work by C.H. was supported by the grants of National Research Foundation of Korea (2019R1A2C2085965 and 2020R1A4A2002885). This work was conducted during the research year of Chungbuk National University in 2021. This research has made use of the KMTNet system operated by the Korea Astronomy and Space Science Institute (KASI) and the data were obtained at three host sites of CTIO in Chile, SAAO in South Africa, and SSO in Australia. The OGLE project has received funding from the National Science Centre, Poland, grant MAESTRO 2014/14/A/ST9/00121 to AU.

References

Alard, C., & Lupton, R. H. 1998, ApJ, 503, 325
Albrow, M. 2017, `https://doi.org/10.5281/zenodo.268049`
Albrow, M., Horne, K., Bramich, D. M., et al. 2009, MNRAS, 397, 2099
Alcock, C., Akerlof, C. W., Allsman, R. A., et al. 1993, Nature, 365, 621
An, J. H., & Han, C. 2002, ApJ, 573, 351
Aubourg, E., Bareyre, P., Bréhin, S., et al. 1993, Nature, 365, 623
Batista, V., Gould, A., Dieters, S., et al. 2011, A&A, 529, A102
Bennett, D. P., Bond, I. A., Udalski, A., et al. 2008, ApJ, 684, 663B
Bensby, T., Yee, J. C., Feltzing, S., et al. 2013, A&A, 549, A14
Bessell, M. S., & Brett, J. M. 1988, PASP, 100, 1134
Claret, A. 2000, A&A, 363, 1081
Di Stefano, R., & Mao, S. 1996, ApJ, 457, 93
Dominik, M. 1998, A&A, 329, 361
Dominik, M. 1999, A&A, 349, 108
Gaudi, B. S. 2012, ARA&A, 50, 411
Gould, A. 1992, ApJ, 392, 442
Gould, A. 2000, ApJ, 542, 785
Gould, A., & Andronov, N. 1999, ApJ, 516, 236
Griest, K., & Safizadeh, N. 1998, ApJ, 500, 37
Han, C., & Gould, A. 1995, ApJ, 447, 53
Han, C., & Gould, A. 2003, ApJ, 592, 172
Han, C., Kim, D., Udalski, A., et al. 2020a, AJ, 160, 64
Han, C., Shin, I.-G., Jung, Y. K., et al. 2020b, A&A, 641, A105
Han, C., Udalski, A., Kim, D., et al. 2021a, A&A, 642, A110
Han, C., Udalski, A., Kim, D., et al. 2021b, A&A, 650, A89
Han, C., Udalski, A., Kim, D., et al. 2021c, A&A, 649, A90
Holtzman, J. A., Watson, A. M., Baum, W. A., et al. 1998, AJ, 115, 1946
Jung, Y. K., Udalski, A., Gould, A., et al. 2018, AJ, 155, 219
Jung, Y. K., Han, C., Udalski, A., et al. 2021, AJ, 161, 293
Kervella, P., Thévenin, F., Di Folco, E., & Ségransan, D. 2004, A&A, 426, 29
Kim, S.-L., Lee, C.-U., Park, B.-G., et al. 2016, J. Korean Astron. Soc., 49, 37
Mróz, P., Han, C., Udalski, A., et al. 2017, AJ, 153, 143
Nataf, D. M., Gould, A., Fouqué, P., et al. 2013, ApJ, 769, 88
Robin, A. C., Reylé, C., Derriére, S., & Picaud, S. 2003, A&A, 409, 523
Sumi, T., Bennett, D. P., Bond, I. A., et al. 2013, ApJ, 778, 150
Tomaney, A. B., & Crotts, A. P. S. 1996, AJ, 112, 2872
Udalski, A., Szymański, M., Kałużny, J., et al. 1993, Acta Astron., 43, 289
Udalski, A., Szymański, M., Kałużny, J., et al. 1994, Acta Astron., 44, 1
Udalski, A., Szymański, M. K., & Szymański, G. 2015, Acta Astron., 65, 1
Woźniak, P. R. 2000, Acta Astron., 50, 42
Yee, J. C., Shvartzvald, Y., Gal-Yam, A., et al. 2012, ApJ, 755, 102
Zang, W., Hwang, K.-H., Udalsk, A., et al. 2021, AJ, 162, 163